A Reduced Order Variational Spectral Method for Efficient Construction of Eigenstrain-based Reduced Order Homogenization Models

Aslan Nasirov and Caglar Oskay*
Department of Civil and Environmental Engineering
Vanderbilt University
Nashville, TN 37235, USA

Abstract

Reduced order models (ROMs) are often coupled with concurrent multiscale simulations to mitigate the computational cost of nonlinear computational homogenization methods. Construction (or training) of ROMs typically requires evaluation of a series of linear or nonlinear equilibrium problems, which itself could be a computationally very expensive process. In the eigenstrain-based reduced order homogenization method (EHM), a series of linear elastic microscale equilibrium problems are solved to compute the localization and interaction tensors that are in turn used in the evaluation of the reduced order multiscale system. These microscale equilibrium problems are typically solved using either the finite element method or semi-analytical methods. In the present study, a reduced order variational spectral method is developed for efficient computation of the localization and interaction tensors. The proposed method leads to a small stiffness matrix that scales with the order of the reduced basis rather than the number of degrees of freedom in the finite element mesh. The reduced order variational spectral method maintains high accuracy in the computed response fields. A speedup higher than an order of magnitude can be achieved compared to the finite element method in polycrystalline microstructures. The accuracy and scalability of the method for large polycrystals and increasing phase property contrast are investigated.

1 Introduction

Computational homogenization method [1] applied to heterogeneous materials that exhibit material nonlinearities leads to coupled and nested macroscale and microscale boundary value problems

*Corresponding Author. Email: caglar.oskay@vanderbilt.edu

(BVPs) defined over the structural domain and representative microstructural volumes, respectively. Macroscale BVP is commonly solved using the finite element method, while microscale BVPs have been evaluated using various full-field methods such as the finite element method (also known as FE^2 method [1]), virtual element method [2], spectral methods [3, 4], among others. Among these full-field methods, the spectral approach is advantageous because of its computational efficiency.

The spectral method proposed by Moulinec and Suquet has introduced application of fast Fourier transform (FFT) algorithms to multiscale problems [3, 5, 6]. This spectral formulation relies on Lippmann-Schwinger type multiscale ansatz which is expressed as

$$\epsilon_{ij}(\boldsymbol{y}) = \bar{\epsilon}_{ij} - \int_{\Theta} \Gamma_{ijkl}(\boldsymbol{y}, \hat{\boldsymbol{y}})(L_{klmn}(\hat{\boldsymbol{y}}) - L^0_{klmn})\epsilon_{mn}(\hat{\boldsymbol{y}})d\hat{\boldsymbol{y}} \tag{1}$$

where $\boldsymbol{\epsilon}$ is the strain field over the microstructure volume denoted as Θ, $\bar{\boldsymbol{\epsilon}}$ is the macroscale strain tensor, $\boldsymbol{y}$ is the position vector defined over the microstructure volume, $\boldsymbol{\Gamma}$ is the kernel function, and $\boldsymbol{L}^0$ is a reference stiffness. Introduction of reference stiffness allows for the analytical derivation of the kernel function in the frequency space such that stress equilibrium and strain compatibility are enforced. For microstructures where the constituents have high property contrast, further methodological developments focused on accelerating convergence using the augmented Lagrangian approach [7] and resolving Gibbs phenomenon [8]. Comprehensive reviews on recent developments and applications of the spectral method in solving the microscale problem are provided in Refs. [9, 10, 11].

More recently, Zeman et al. [12] and Geus et al. [13] have introduced the variational spectral method eliminating the need for selection of a reference stiffness which affects rate of convergence [3]. In this formulation, the governing equations are solved directly for strains. Strain compatibility is enforced using projection operators for which analytical expressions were derived in the frequency space by Milton and Kohn [14]. Discretization of the strain field is carried out using trigonometric polynomials instead of Lagrange polynomials often used in classical finite element methods. The resulting linear system is then iteratively solved using FFT algorithms.

Despite the aforementioned advancements in efficient computation of the full-field solution of the microscale BVP, application of computational homogenization to realistic-size heterogeneous structures remain to be prohibitively expensive. Therefore, significant effort has been devoted to the development of reduced order models (ROMs) that drastically speed up the evaluation of the microscale BVP while attempting to preserve prediction accuracy. Various ROM approaches have been proposed, including the transformation field analysis (TFA) [15, 16], nonuniform TFA (NTFA) [17, 18, 19, 20] and its extensions [21, 22, 23], numerical potentials [24], self-consistent clustering analysis [25], eigendeformation and eigenstrain-based reduced order homogenization [26, 27, 28, 29, 30, 31, 32], surrogate models [33, 34, 35], and proper orthogonal decomposition (POD) [36, 37, 38]. ROMs typically consist of an off-line model training stage where the ROM is constructed based on prior simulations, and a model execution stage, where the solution is searched over a coarse

approximation space spanned by a small set of basis functions. By definition, model execution is computationally efficient, and is coupled to the macroscopic solver by replacing the full field solution of the microscale BVP. Approaches that embed the model training stage in model execution have also been explored (see e.g., [39]).

Depending on the size of the microstructure volume and complexity of the morphological features embedded in the volume, model training stage could be computationally very expensive. Several ROM approaches such as NTFA and POD-based models, as well as machine learning models rely on a suite of full-field nonlinear microscale simulations for model training. Eigenstrain-based reduced order homogenization method (EHM) [29] is particularly advantageous in this regard since only linear elastic simulations are required to train the model. Specifically, localization and interaction tensors are computed by solving linear-elastic microscale equilibrium problems, denoted as the influence function problems (IFPs). In past studies, the finite element method [29, 40, 41] and the generalized finite element method [42] have been used to solve these IFPs. For microstructures with complex features that require dense meshes and a relatively large set of approximation basis functions, the solution of IFPs can also become computationally intensive [43, 22]. To the best of the authors' knowledge, analytical approximations of the influence functions are not available beyond a few idealized microstructures (e.g., ellipsoidal inclusions), although the relationship between the Lippmann-Schwinger ansatz and the interaction tensors has been recently explored by Buryachenko [44]. Alternatively, self-consistent or Mori-Tanaka [45, 46] type analytical methods have been used to estimate the localization and interaction tensors, but at the expense of introducing assumptions on phase geometry and simplifications of phase-to-phase interactions as shown in Dvorak's pioneering work [15, 16].

The EHM approach has been previously applied to investigate complex multiscale applications, and validated against experimental data. For instance, Zhang et al. [47] applied EHM to multiscale thermostructural modeling of titanium skin panels. This study showed the ability of the ROM to conduct full concurrent nonlinear multiscale simulations that are otherwise prohibitively expensive using traditional nonlinear computational homogenization. Zhang et al. [48] used the ROM to predict probabilistic fatigue life of titanium polycrystals including comparison to experimentally observed fatigue life. The results suggested that the ROM can be used to capture the evolution of fatigue initiation parameters over thousands of polycrystal statistical volume elements and load cycles. Nasirov et al. [43] compared stress-strain response of the ROM to experimentally-calibrated crystal plasticity finite element results for additively-manufactured Inconel alloys.

In the present study, we propose a new computational strategy to speed up the model training stage for EHM. The proposed strategy leverages the aforementioned ideas on the variational spectral method (VSM) to directly compute the localization and interaction tensors without the need for first evaluating the influence function problems. In this regard, the part-average localization tensors are treated as the cardinal unknowns and a variational form through the VSM is obtained. Unlike the

classical finite element or VSM, where the degrees of freedom scale with the underlying discretization, the proposed approach scales with the order of the reduced basis, which is much smaller. The accuracy and efficiency of the new computational strategy is assessed by comparing model predictions to those obtained by the finite element analysis. While the proposed approach is general and different microstructure morphologies and material behavior could be incorporated into the framework, the numerical assessment is performed using polycrystalline microstructures that represent a wide range of materials including metals and alloys [49, 50], molecular crystals [51, 52], among others. The primary contribution of the present work is in the development of a reduced order version of the variational spectral method, and its application to the offline stage of the EHM. A significant majority of the reduced order modeling research have focused on the ROM execution stage, whereas efficiency in ROM construction has received relatively less attention. Direct numerical simulations (using finite elements or spectral methods) that are typically used to construct/train ROMs are often computationally very expensive, which motivated the current effort. In particular, the proposed approach makes the EHM model construction more efficient by reduced-basis approximation of the generalized polarization strains.

This manuscript is organized as follows: The EHM methodology is briefly summarized in Section 2. The mathematical formulation for the proposed spectral method to evaluate the polarization and interaction tensors is developed in Section 3. Numerical experiments performed to assess the accuracy and efficiency of the method are discussed in Section 4. The localization and interaction tensors are compared to those computed directly using the finite element method as described in Ref. [29]. Conclusions drawn are summarized and discussed in Section 5.

The following notation is used unless otherwise stated. Scalars are denoted by lightface letters, α, Cartesian tensor fields are denoted as italic lightface letters, A_{ijkl} (or σ_{ij}), in indicial notation with italic indices, $ijkl$ (or ij), and referred to as boldface italic, $\boldsymbol{A}$ (or $\boldsymbol{\sigma}$), in text/tensor notation. A comma in the indices indicates partial spatial derivative. The top right superscript is used as a descriptor. Overbar indicates macroscopic quantity averaged over the microstructural domain while overhead dot indicates time derivative. The $*$ symbol indicates convolution.

2 EHM Overview

Consider a macroscopic domain, $\Omega \subset \mathbb{R}^3$, that is made of periodic polycrystalline microstructural domain, $\Theta \subset \mathbb{R}^3$. A classical two-scale homogenization procedure (see [29] for details) for elastostatics leads to two boundary value problems defined over the macroscale domain and the microscale domain (e.g., a representative volume element or a statistical volume element). The macroscale boundary

value problem in the absence of inertial forces is given by

$$\bar{\sigma}_{ij,j}(\boldsymbol{x},t) + \bar{b}_i(\boldsymbol{x},t) = 0 \tag{2}$$

$$\bar{\epsilon}_{ij}(\boldsymbol{x},t) = \frac{1}{2}(\bar{u}_{i,j}(\boldsymbol{x},t) + \bar{u}_{j,i}(\boldsymbol{x},t)) \tag{3}$$

$$\bar{u}_i(\boldsymbol{x},t) = \bar{u}_i^*(\boldsymbol{x},t) \quad \boldsymbol{x} \in \Gamma_{\mathrm{u}} \tag{4}$$

$$\bar{\sigma}_{ij}(\boldsymbol{x},t)\hat{n}_j = \bar{t}_i^*(\boldsymbol{x},t) \quad \boldsymbol{x} \in \Gamma_{\mathrm{t}} \tag{5}$$

where $\bar{\boldsymbol{\sigma}}$ denotes the macroscale stress field, $\bar{\boldsymbol{b}}$ denotes the macroscale body forces, $\bar{\boldsymbol{\epsilon}}$ is the macroscopic strain, $\bar{\boldsymbol{u}}$ denotes the macroscale deformation field, $\bar{\boldsymbol{u}}^*$ is the prescribed displacement over Dirichlet boundaries, Γ_{u}, $\bar{\boldsymbol{t}}^*$ is the prescribed traction over Neumann boundaries, Γ_{t}, $\hat{\boldsymbol{n}}$ is the normal vector, and $\boldsymbol{x} \in \Omega$ denotes the macroscale spatial position vector. Using the EHM procedure [29], the microscale homogenized equilibrium equation and the stress-strain relationship along with piece-wise constant reduced order basis functions leads to the following relations

$$\dot{\sigma}_{ij}^{(\beta)}(t) = L_{ijkl}^{(\beta)}\left(\dot{\epsilon}_{kl}^{(\beta)}(t) - \dot{\mu}_{kl}^{(\beta)}(t)\right) \tag{6}$$

$$\dot{\epsilon}_{ij}^{(\beta)}(t) = A_{ijkl}^{(\beta)}\dot{\bar{\epsilon}}_{kl}(t) + \sum_{\alpha=1}^{N_{\mathrm{ph}}} P_{ijkl}^{(\beta\alpha)}\dot{\mu}_{kl}^{(\alpha)}(t) \tag{7}$$

where α and β $(= 1, 2, \ldots, N_{\mathrm{ph}})$ represent part indices, $\boldsymbol{L}^{(\beta)}$ stands for the tensor of elastic moduli for part β, $\boldsymbol{P}^{(\beta\alpha)}$ represents the interaction tensor between parts α and β, $\boldsymbol{A}^{(\beta)}$ stands for the localization tensor averaged over part β, $\boldsymbol{\mu}^{(\beta)}$ is part-averaged viscoplastic strain, $\boldsymbol{\sigma}^{(\beta)}$ is part-averaged stress, $\bar{\boldsymbol{\epsilon}}$ stands for the macroscopic strain, and N_{ph} is the number of basis functions (or parts) used in the reduced order model. The parts are subdomains in the microstructural volume and each part is typically chosen to coincide with a single grain domain (further subpartitioning can be employed). Macroscale position dependence in Eqs. 6 and 7 is suppressed for simplicity since the part-average stress evolution is treated as a constitutive update in the numerical implementation of the multiscale model. Coefficient tensors ($\boldsymbol{A}^{(\beta)}$, $\boldsymbol{L}^{(\beta)}$ and $\boldsymbol{P}^{(\beta\alpha)}$) retain information about the microstructure such as the elastic properties of grains, grain orientation, grain morphology, and grain-to-grain interactions. Combined with appropriate evolution laws for the viscoplastic strain, $\dot{\boldsymbol{\mu}}^{(\beta)}$, stress update procedure is employed to evaluate the reduced order microscale problem [29, 43].

The "model training" stage consists of preparation of the $\boldsymbol{A}^{(\beta)}$ and $\boldsymbol{P}^{(\beta\alpha)}$ tensors by solving linear-elastic microscale equilibrium problems called influence function problems (IFPs). The IFP for the localization tensors is given as

$$\left[L_{ijkl}(\boldsymbol{y})(I_{klmn} + H_{(k,l)mn}(\boldsymbol{y}))\right]_{,j} = 0; \quad \boldsymbol{y} \in \Theta \tag{8a}$$

$$H_{mkl}(\boldsymbol{y}) = 0; \quad \boldsymbol{y} \in \partial\Theta^{\mathrm{v}} \tag{8b}$$

$$H_{mkl}(\boldsymbol{y}) = H_{mkl}(\boldsymbol{y} + \tilde{\boldsymbol{y}}) \quad \boldsymbol{y} \in \partial\Theta^{\mathrm{fe}} \tag{8c}$$

where $\boldsymbol{H}$ is the influence function, $\partial\Theta^{\mathrm{v}}$ represents vertices of the microstructure volume, $\tilde{\boldsymbol{y}}$ stands for the period of the microstructure volume and $\partial\Theta^{\mathrm{fe}}$ represents the faces and edges of the microstructure volume. The influence function is fixed at the vertices of the microstructure volume to eliminate rigid body motion, and periodic boundary conditions are enforced along the faces and edges of the microstructure volume. The localization tensors are expressed using the influence functions as

$$A^{(\beta)}_{ijkl} = \frac{1}{|\Theta^{(\beta)}|}\int_{\Theta} N^{(\beta)}(\boldsymbol{y}) G_{ijkl}(\boldsymbol{y}) d\boldsymbol{y} + I_{ijkl} \tag{9}$$

in which $G_{ijkl} = H_{(i,j)kl}$ and $N^{(\beta)}$ is the indicator function which acts as the reduced order basis function ($N^{(\beta)}(\boldsymbol{y}) = 1$ if $\boldsymbol{y} \in \Theta^{(\beta)}$ and 0 elsewhere).

The IFPs for the interactions tensors are given as (for each $\alpha = 1, 2, \ldots, N_{\mathrm{ph}}$)

$$\left[L_{ijmn}(\boldsymbol{y})\left(h^{(\alpha)}_{(m,n)kl}(\boldsymbol{y}) - I_{mnkl}N^{(\alpha)}(\boldsymbol{y})\right)\right]_{,j} = 0; \quad \boldsymbol{y} \in \Theta \tag{10a}$$

$$h^{(\alpha)}_{mkl}(\boldsymbol{y}) = 0; \quad \boldsymbol{y} \in \partial\Theta^{\mathrm{v}} \tag{10b}$$

$$h^{(\alpha)}_{mkl}(\boldsymbol{y}) = h^{(\alpha)}_{mkl}(\boldsymbol{y} + \tilde{\boldsymbol{y}}) \quad \boldsymbol{y} \in \partial\Theta^{\mathrm{fe}} \tag{10c}$$

where $\boldsymbol{h}^{(\alpha)}$ is the phase influence function associated with part, α. Boundary conditions of the interaction IFPs are the same as those used for the localization IFP. The interaction tensors are expressed using the influence functions as

$$P^{(\beta\alpha)}_{ijkl} = \frac{1}{|\Theta^{(\beta)}|}\int_{\Theta} N^{(\beta)}(\boldsymbol{y}) g^{(\alpha)}_{ijkl}(\boldsymbol{y}) d\boldsymbol{y} \tag{11}$$

with $g^{(\alpha)}_{ijkl} = h^{(\alpha)}_{(i,j)kl}$.

During the construction stage of the ROM, Eq. 8a is solved for $\boldsymbol{H}$ using a numerical method (e.g. finite element method) and the solution field is integrated according to Eq. 9 to compute the localization tensors $\boldsymbol{A}^{(\alpha)}$. Equation 10a is solved for $\boldsymbol{h}^{(\alpha)}$ where α indicates part index and then Eq. 11 is used to arrive at interaction tensors $\boldsymbol{P}^{(\beta\alpha)}$. The cost of solving a single IFP therefore scales with the number of degrees of freedom used in the numerical method, N_{dof}. On the other hand, solving Eq. 11 requires solving $6\,N_{\mathrm{ph}}$ linear-elastic problems in three dimensions. N_{ph} can be relatively large for polycrystals with large number of grains [43], composites with large number of randomly oriented short fibers [25], concrete microstructure with irregular inclusions, etc. Even in the case of relatively simple microstructures, additional parts may need to be added at material interfaces, triple junctions, and near other stress risers to capture the behavior more accurately using the ROM [31]. Furthermore, the discretization around inclusions, cracks, defects or grain boundaries typically needs to be very fine to capture discontinuities leading to higher N_{dof}. In such cases, solving for the coefficient tensors becomes computationally expensive.

3 Reduced order variational spectral method

In what follows a reduced order spectral method for solving the IFPs described by Eqs. 8a and 10a is formulated. First, we formulate the spectral method for solving Eq. 8a in detail due to its relative simplicity. The formulation is then generalized to address the IFPs for the interaction tensors.

3.1 Localization tensor

The strong form of the influence function problem is brought to the weak form by employing the classical variational procedure

$$\int_{\Theta} w_{ij}(\boldsymbol{y}) L_{ijkl}(\boldsymbol{y}) A_{klmn}(\boldsymbol{y}) d\boldsymbol{y} = \int_{\partial\Theta} v_i(\boldsymbol{y}) L_{ijkl}(\boldsymbol{y}) A_{klmn}(\boldsymbol{y}) n_j d\boldsymbol{y} \tag{12}$$

where $\boldsymbol{A} = \boldsymbol{G} + \boldsymbol{I}$, $\boldsymbol{v}$ is the test function, $\boldsymbol{w} = \nabla^s \boldsymbol{v}$ the symmetric gradient of the test function, $\partial\Theta$ denotes the exterior boundaries of the microstructural volume, and $\boldsymbol{n}$ is the outward unit normal to the exterior boundaries. The boundary term vanishes by the use of periodicity conditions. Equation 12 is then expressed as

$$\int_{\Theta} w_{ij}(\boldsymbol{y}) L_{ijkl}(\boldsymbol{y}) G_{klmn}(\boldsymbol{y}) d\boldsymbol{y} = -\int_{\Theta} w_{ij}(\boldsymbol{y}) L_{ijmn}(\boldsymbol{y}) d\boldsymbol{y}. \tag{13}$$

Substituting $G_{klmn} = H_{(k,l)mn}$ we arrive at the weak form of the Eq. 8a

$$\int_{\Theta} w_{ij}(\boldsymbol{y}) L_{ijkl}(\boldsymbol{y}) H_{(k,l)mn}(\boldsymbol{y}) d\boldsymbol{y} = -\int_{\Theta} w_{ij}(\boldsymbol{y}) L_{ijmn}(\boldsymbol{y}) d\boldsymbol{y}. \tag{14}$$

Following the standard finite element procedure, solution to the weak form in Eq. 14 can be obtained as described in Ref. [29]. In contrast, we seek to directly solve the weak form in Eq. 13 for the polarization strains, $\boldsymbol{G}$, using VSM, while satisfying compatibility and zero-mean property of the polarization strains. Compatibility of the polarization strains can be expressed in two alternative forms

$$G_{ijmn,kl}(\boldsymbol{y}) - G_{kjmn,il}(\boldsymbol{y}) - G_{ilmn,kj}(\boldsymbol{y}) + G_{klmn,ij}(\boldsymbol{y}) = 0 \tag{15}$$

$$G_{ijmn}(\boldsymbol{y}) = H_{(i,j)mn}(\boldsymbol{y}) \tag{16}$$

The first form shown in Eq. 15 is the classical compatibility equation [53], whereas the second form in Eq. 16 corresponds to the observation that the polarization strain is obtained as the gradient of a function that satisfies the standard continuity conditions of a displacement field. When evaluating Eq. 14 using the FEM, compatibility is satisfied since Eq. 16 is directly employed. In the current formulation, we employ Eq. 15 to enforce compatibility.

The zero-mean property of the polarization strain can be stated as

$$\int_{\Theta} G_{ijmn}(\boldsymbol{y}) d\boldsymbol{y} = \int_{\Theta} H_{(i,j)mn}(\boldsymbol{y}) d\boldsymbol{y} = \int_{\partial\Theta} H_{imn}(\boldsymbol{y}) n_j(\boldsymbol{y}) d\boldsymbol{y} = 0. \tag{17}$$

When evaluating Eq. 14 using the FEM, Eq. 17 is satisfied due to the periodicity of the elastic influence function, $\boldsymbol{H}$ along the boundary conditions of the microstructure volume. In the current formulation, the zero mean property of the polarization strain is enforced as a direct constraint. Considering the microstructural equilibrium, compatibility and the zero mean property, the strong-form microscale problem in Eq. 8a is recast using the following equations ($\boldsymbol{y} \in \Theta$)

$$\left[L_{ijkl}(\boldsymbol{y})(I_{klmn} + G_{klmn}(\boldsymbol{y}))\right]_{,j} = 0; \tag{18a}$$

$$G_{ijmn,kl}(\boldsymbol{y}) - G_{kjmn,il}(\boldsymbol{y}) - G_{ilmn,kj}(\boldsymbol{y}) + G_{klmn,ij}(\boldsymbol{y}) = 0 \tag{18b}$$

$$\int_{\Theta} G_{ijmn}(\boldsymbol{y}) d\boldsymbol{y} = 0 \tag{18c}$$

where the polarization strain field, $\boldsymbol{G}$, is taken to be the cardinal unknown field.

Following Zeman et al. [12], we define generalized test functions, $\boldsymbol{w}^\star$, and trial functions, $\boldsymbol{G}^\star$, such that

$$w_{ij}(\boldsymbol{y}) = \int_{\Theta} \Gamma_{ijkl}(\boldsymbol{y} - \hat{\boldsymbol{y}}) w^\star_{kl}(\hat{\boldsymbol{y}}) d\hat{\boldsymbol{y}} = \Gamma_{ijkl} * w^\star_{kl} \tag{19}$$

$$G_{klmn}(\boldsymbol{y}) = \int_{\Theta} \Gamma_{klrs}(\boldsymbol{y} - \hat{\boldsymbol{y}}) G^\star_{rsmn}(\hat{\boldsymbol{y}}) d\hat{\boldsymbol{y}} = \Gamma_{klrs} * G^\star_{rsmn} \tag{20}$$

where $\boldsymbol{w}^\star$ and $\boldsymbol{G}^\star$ are generalized incompatible tensor fields with non-zero mean that are mapped into $\boldsymbol{w}$ and $\boldsymbol{G}$ (compatible parts) using the operator $\boldsymbol{\Gamma}$. The operator $\boldsymbol{\Gamma}$ enforces compatibility and zero-mean property, and is given by Milton and Kohn [14] in frequency space as follows

$$\hat{\Gamma}_{ijkl} = \frac{1}{2\|\xi\|^2}(\xi_i\xi_k\delta_{jl} + \xi_i\xi_l\delta_{jk} + \xi_j\xi_k\delta_{il} + \xi_j\xi_l\delta_{ik}) - \frac{1}{\|\xi\|^4}\xi_i\xi_j\xi_k\xi_l \quad \forall \boldsymbol{\xi} \neq 0 \tag{21}$$

where $\boldsymbol{\xi}$ is the frequency vector. For completeness, derivation of the kernel is included in Appendix A.

Substituting Eq. 20 into Eq. 13 yields

$$\int_{\Theta} \left[w^\star_{ab} * \Gamma_{ijab}\right] \, L_{ijkl} \, \left[\Gamma_{klrs} * G^\star_{rsmn}\right] d\boldsymbol{y} = -\int_{\Theta} \left[w^\star_{ab} * \Gamma_{ijab}\right] L_{ijmn} d\boldsymbol{y}. \tag{22}$$

We proceed by exploiting the self-adjoint property of the operator $\boldsymbol{\Gamma}$ which results in

$$\int_{\Theta} w^\star_{ab} \Gamma_{ijab} * \left[L_{ijkl}\left[\Gamma_{klrs} * G^\star_{rsmn}\right]\right] d\boldsymbol{y} = -\int_{\Theta} \left[w^\star_{ab} * \Gamma_{ijab}\right] L_{ijmn} d\boldsymbol{y}. \tag{23}$$

Equation 23 represents a continuous weak form for the incompatible trial and test strains. We proceed with a reduced order discretization of the incompatible trial and test strains using indicator functions as follows

$$w^\star_{ij}(\boldsymbol{y}) = \sum_{\alpha} N^{(\alpha)}(\boldsymbol{y}) w^{\star,(\alpha)}_{ij} \tag{24}$$

$$G^\star_{ijmn}(\boldsymbol{y}) = \sum_{\beta} N^{(\beta)}(\boldsymbol{y}) G^{\star,(\beta)}_{ijmn} \tag{25}$$

where $\boldsymbol{w}^{\star,(\alpha)}$ and $\boldsymbol{G}^{\star,(\beta)}$ are given as

$$w_{ij}^{\star,(\alpha)} = \frac{1}{|\Theta^{(\alpha)}|}\int_{\Theta} N^{(\alpha)}(\boldsymbol{y}) w_{ij}^{\star}(\boldsymbol{y}) d\boldsymbol{y} \tag{26}$$

$$G_{ijmn}^{\star,(\beta)} = \frac{1}{|\Theta^{(\beta)}|}\int_{\Theta} N^{(\beta)}(\boldsymbol{y}) G_{ijmn}^{\star}(\boldsymbol{y}) d\boldsymbol{y}. \tag{27}$$

The indicator functions above are defined as

$$N^{(\alpha)}(\boldsymbol{y}) = \begin{cases} 1 & \boldsymbol{y} \in \Theta^{(\alpha)} \\ 0 & \boldsymbol{y} \notin \Theta^{(\alpha)} \end{cases} \tag{28}$$

where $\Theta^{(\alpha)}$ is the subdomain of the microstructure (referred to as "part"). Using indicator functions as basis functions results in C^{-1} continuous incompatible strains, which provides the same order of continuity for the generalized polarization strain field as is the case for standard finite element shape functions. The coefficients $\boldsymbol{w}^{\star,(\alpha)}$ and $\boldsymbol{G}^{\star,(\alpha)}$ can be physically interpreted as average incompatible strains within part α (such that $\Theta^{(\alpha)} \subseteq \Theta$). For single-phase polycrystalline microstructures, part-per-grain discretization (that is a single part is assigned to the domain of each grain within the microstructure) have been found to provide efficient and accurate reduced order approximation with EHM [29, 40]. Verification examples below consider models based on part-per-grain discretization.

Substituting the discretized incompatible test and trial functions and the indicator functions into the weak form results in

$$\sum_{\alpha}\sum_{\beta} w_{ab}^{\star,(\alpha)} \int_{\Theta^{(\alpha)}} \Gamma_{ijab} * \left[L_{ijkl}\left[\Gamma_{klrs} * N^{(\beta)}\right]\right] d\boldsymbol{y}\, G_{rsmn}^{\star,(\beta)} = -\sum_{\alpha} w_{ab}^{\star,(\alpha)} \int_{\Theta} \left[\Gamma_{ijab} * N^{(\alpha)}\right] L_{ijmn} d\boldsymbol{y} \tag{29}$$

Renaming the integrals on the left and right hand side of Eq. 29 and considering arbitrary incompatible test functions, Eq. 29 is expressed in the simple form

$$\sum_{\beta} K_{abrs}^{(\alpha\beta)}\, G_{rsmn}^{\star,(\beta)} = F_{abmn}^{(\alpha)}; \quad \alpha = 1, 2, \ldots, N_{\text{ph}} \tag{30}$$

In matrix notation, Eq. 30 is expressed as follows

$$\begin{bmatrix} \boldsymbol{K}^{(11)} & \boldsymbol{K}^{(12)} & \ldots & \boldsymbol{K}^{(1N_{\text{ph}})} \\ \boldsymbol{K}^{(21)} & \boldsymbol{K}^{(22)} & \ldots & \boldsymbol{K}^{(2N_{\text{ph}})} \\ \vdots & \vdots & \ddots & \vdots \\ \boldsymbol{K}^{(N_{\text{ph}}1)} & \boldsymbol{K}^{(N_{\text{ph}}2)} & \ldots & \boldsymbol{K}^{(N_{\text{ph}}N_{\text{ph}})} \end{bmatrix} \begin{bmatrix} \boldsymbol{G}^{\star(1)} \\ \boldsymbol{G}^{\star(2)} \\ \vdots \\ \boldsymbol{G}^{\star(N_{\text{ph}})} \end{bmatrix} = \begin{bmatrix} \boldsymbol{F}^{(1)} \\ \boldsymbol{F}^{(2)} \\ \vdots \\ \boldsymbol{F}^{(N_{\text{ph}})} \end{bmatrix} \tag{31}$$

The incompatible strain polarization coefficients, $\boldsymbol{G}^{\star}$, are obtained from Eq. 31, and the localization tensors are reconstructed using the operator, $\boldsymbol{\Gamma}$ as

$$A_{ijmn}(\boldsymbol{y}) = G_{ijmn} + I_{ijmn} = \sum_{\alpha} \Gamma_{ijrs}^{(\alpha)}(\boldsymbol{y}) G_{rsmn}^{\star,(\alpha)} + I_{ijmn} \tag{32}$$

$$A_{ijmn}^{(\beta)} = \sum_{\alpha} \Gamma_{ijrs}^{(\beta\alpha)} G_{rsmn}^{\star,(\alpha)} + I_{ijmn} \tag{33}$$

where,

$$\Gamma^{(\alpha)}_{ijmn}(\boldsymbol{y}) = \left[\Gamma_{ijmn} * N^{(\alpha)}\right](\boldsymbol{y}) \tag{34}$$

$$\Gamma^{(\beta\alpha)}_{ijmn} = \frac{1}{|\Theta^{(\beta)}|}\int_{\Theta} N^{(\beta)}(\boldsymbol{y})\Gamma^{(\alpha)}_{ijmn}(\boldsymbol{y})d\boldsymbol{y}. \tag{35}$$

Direct evaluation of the localization tensors using the formulation described above has two key benefits. (1) The size of the sub-matrices, $\boldsymbol{K}^{(\alpha\beta)}$ and the overall size of the stiffness matrix, $\boldsymbol{K}$ are 6×6 and $6N_{\text{ph}}\times 6N_{\text{ph}}$, respectively. The size of the system of equations in Eq. 31 is small given that it is dictated by the number of reduced order basis functions. (2) Periodicity is enforced through the kernel operator, eliminating the need to directly enforce boundary constraints through tedious procedures such as the master-slave approach.

The system of equations shown in Eq. 31 ($\boldsymbol{K}\boldsymbol{G}^{\star} = \boldsymbol{F}$) is rank deficient and possesses infinitely many solutions since the strain compatibility and the zero mean conditions (Eqs. 18b and 18c) are not enforced. However, when any given incompatible solution that satisfies Eq. 31 is passed through the operator, $\boldsymbol{\Gamma}$, a unique polarization strain field is recovered. As described in Appendix A, the operator $\boldsymbol{\Gamma}$ projects the incompatible solutions onto their unique, zero-mean, curl-free part. Therefore, we seek to identify any one of the infinite solutions that satisfy Eq. 31. This could be achieved by employing the least squares (LSTSQ) solver in a straightforward manner. An alternative approach could be using singular value decomposition (SVD) to decompose the stiffness matrix, and then performing $6\times N_{\text{ph}}$ back-substitutions to compute the interaction tensors.

The operator, $\boldsymbol{\Gamma}$, is analytically known in the frequency space. Therefore, the convolutions needed to compute the force and stiffness matrices (see Eq. 29) are evaluated by applying the convolution theorem as follows

$$\Gamma_{ijkl} * N^{(\alpha)} = \mathcal{F}^{-1}\{\hat{\Gamma}_{ijkl}\mathcal{F}\{N^{(\alpha)}\}\} \tag{36}$$

$$\Gamma_{ijab} * [L_{ijkl}\,[\Gamma_{klrs} * N^{(\beta)}]] = \mathcal{F}^{-1}\{\hat{\Gamma}_{ijab}\mathcal{F}\{L_{ijkl}\mathcal{F}^{-1}\{\hat{\Gamma}_{klrs}\mathcal{F}\{N^{(\beta)}\}\}\}\} \tag{37}$$

where $\mathcal{F}$ and $\mathcal{F}^{-1}$ respectively stand for forward and inverse FFT operations. Since $N^{(\alpha)}$ is known, this operation is very efficient due to the superior scaling properties of FFT algorithms. The remainder of the integrals in force and stiffness matrix expressions are evaluated numerically using the piecewise-constant trapezoidal rule.

The cost of the proposed method depends on the way the linear system is constructed and solved. We have used the discrete weak form shown in Eq. 29 to arrive at the linear system (Eq. 31). Upon closer examination, we observe that one needs to perform $36^2\times N_{\text{ph}}$ FFTs and integrate over each partition individually. One alternative derivation is to combine discrete representation of generalized test and trial functions (Eq. 25) and the weak form shown in Eq. 22 to arrive at the following

discrete weak form

$$\sum_{\alpha}\sum_{\beta} w_{ab}^{\star,(\alpha)} \int_{\Theta} \left[N^{(\alpha)} * \Gamma_{ijab}\right] \, L_{ijkl} \, \left[\Gamma_{klrs} * N^{(\beta)}\right] d\boldsymbol{y} G_{rsmn}^{\star,(\beta)} = - \sum_{\alpha} w_{ab}^{\star,(\alpha)} \int_{\Theta} [N^{(\alpha)} * \Gamma_{ijab}] \, L_{ijmn} d\boldsymbol{y}. \quad (38)$$

Using Eq. 38 requires performing $36 \times N_{\text{ph}}$ FFTs and integrating over the entire microstructural domain to arrive at the stiffness matrix in Eq. 31. It is also possible to explore matrix-free iterative methods as shown in Ref. [3, 12] to circumvent the need to construct and store the stiffness matrix altogether.

3.2 Interaction tensors

Following similar arguments and procedure as discussed above, we arrive at the following discretized weak form the IFP for the interaction tensors (i.e., Eq. 10a)

$$\sum_{\alpha}\sum_{\beta} w_{ab}^{\star,(\alpha)} \int_{\Theta^{(\alpha)}} \Gamma_{ijab} * [L_{ijkl} \, [\Gamma_{klrs} * N^{(\beta)}]] d\boldsymbol{y} \, g_{rsmn}^{\star,(\beta\gamma)} = \sum_{\alpha} w_{ab}^{\star,(\alpha)} \int_{\Theta^{(\gamma)}} \Gamma_{ijab}^{(\alpha)} \, L_{ijmn} d\boldsymbol{y}. \quad (39)$$

Discretization of Eq. 39 results in the following system in matrix notation:

$$\begin{bmatrix} \boldsymbol{K}^{(11)} & \boldsymbol{K}^{(12)} & \dots & \boldsymbol{K}^{(1N_{\text{ph}})} \\ \boldsymbol{K}^{(21)} & \boldsymbol{K}^{(22)} & \dots & \boldsymbol{K}^{(2N_{\text{ph}})} \\ \vdots & \vdots & \ddots & \vdots \\ \boldsymbol{K}^{(N_{\text{ph}}1)} & \boldsymbol{K}^{(N_{\text{ph}}2)} & \dots & \boldsymbol{K}^{(N_{\text{ph}}N_{\text{ph}})} \end{bmatrix} \begin{bmatrix} \boldsymbol{g}^{\star(11)} & \dots & \boldsymbol{g}^{\star(1N_{\text{ph}})} \\ \boldsymbol{g}^{\star(21)} & \dots & \boldsymbol{g}^{\star(2N_{\text{ph}})} \\ \vdots & & \vdots \\ \boldsymbol{g}^{\star(N_{\text{ph}}1)} & \dots & \boldsymbol{g}^{\star(N_{\text{ph}}N_{\text{ph}})} \end{bmatrix} = \begin{bmatrix} \boldsymbol{F}^{(11)} & \dots & \boldsymbol{F}^{(1N_{\text{ph}})} \\ \boldsymbol{F}^{(21)} & \dots & \boldsymbol{F}^{(2N_{\text{ph}})} \\ \vdots & & \vdots \\ \boldsymbol{F}^{(N_{\text{ph}}1)} & \dots & \boldsymbol{F}^{(N_{\text{ph}}N_{\text{ph}})} \end{bmatrix} \quad (40)$$

in which, the matrix entries, $\boldsymbol{K}^{(\beta\gamma)}$, $\boldsymbol{g}^{\star,(\beta\gamma)}$ and $\boldsymbol{F}^{(\beta\gamma)}$ respectively denote the stiffness, unknown and force sub-matrices. Hence, in 3D, the size of each sub-matrix is 6×6. The system of linear equations are evaluated for the incompatible $\boldsymbol{g}^{\star,(\beta\gamma)}$ tensors. It is worthy of note that the stiffness matrix in Eq. 40 is identical to that in Eq. 31. Therefore, the two systems can be combined to solve for $6 \times (N_{\text{ph}} + 1)$ unknown coefficients of the localization and interaction tensors.

Extraction of the compatible part of the interaction tensors is then performed as follows

$$P_{ijmn}^{(\beta\gamma)} := g_{ijmn}^{(\beta\gamma)} = \sum_{\alpha} \Gamma_{ijrs}^{(\beta\alpha)} g_{rsmn}^{\star,(\alpha\gamma)}. \quad (41)$$

The simplicity of Eq. 41 is because the same discretization is adopted in the spectral method as in the partitioning used in the ROM. In general, it is possible to adopt separate discretizations in the evaluation of the interactions tensors and ROM partitioning. A possible motivation for adopting separate discretizations could be to improve the accuracy of coefficient tensor computation (by using a more refined partitioning for the spectral method) at some additional cost.

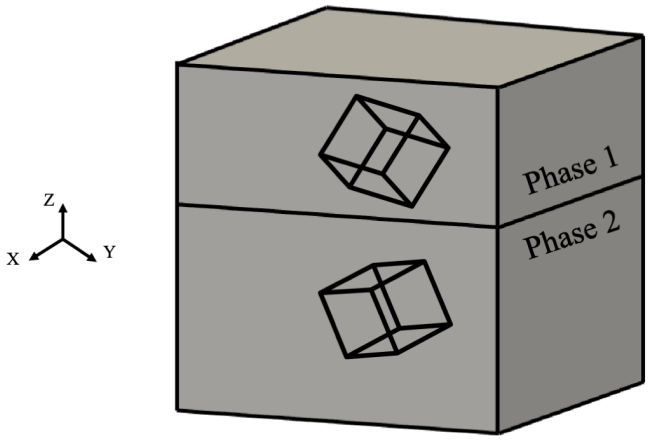

Figure 1: 2-grain polycrystal geometry.

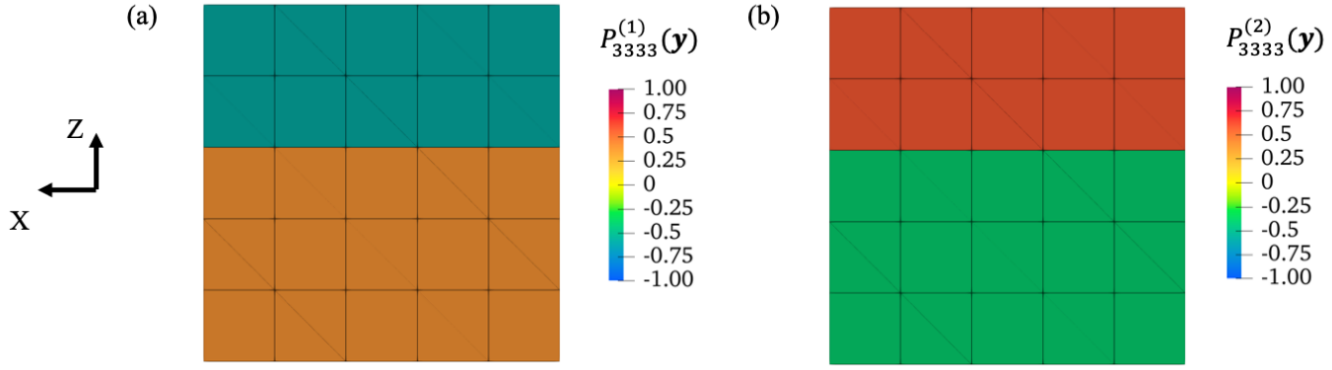

Figure 2: a) Computed interaction field, $P^{(1)}_{3333}(\boldsymbol{y})$, and b) computed interaction field, $P^{(2)}_{3333}(\boldsymbol{y})$.

4 Numerical experiments

The accuracy of the proposed spectral method as well as the scalability with respect to number of grid points and number of phases in the microstructure is assessed using numerical examples. Microstructures were generated using the Neper software [54]. Generated microstructures are voxel images and can be directly used as input to the spectral method, which employs voxel-based discretization needed for the Fast Fourier transforms in Eqs. 36 and 37. The solution of the IFPs using the finite element method (FEM) serves as the basis of accuracy and scalability assessment. In the FEM simulations, each voxel is split into six linear tetrahedral elements, and periodicity is enforced as described in Ref. [29]. The reference code has been implemented in Fortran, while the spectral method is implemented as a Python script using Numpy [55], Scipy [56], and Numba [57] libraries. The reference simulations therefore have a speed advantage over the proposed approach due to the speed differences between the programming languages.

The accuracy of the proposed spectral method relative to FEM is quantified based on the average

$e(\boldsymbol{G}^{(\beta)})$	$e(\boldsymbol{P}^{(\beta\alpha)})$	$e(\overline{\boldsymbol{L}})$
3.48436E-04 %	6.44938E-06 %	2.92416E-05 %

Table 1: 2-grain case: errors in polarization, interaction tensors and homogenized moduli.

error measure, e, for some tensorial quantity, $\boldsymbol{B}^{\mathrm{Sp}}$, computed using following formula

$$e(\boldsymbol{B}^{\mathrm{Sp}}) = \frac{\sqrt{\sum_{\alpha\beta\ldots,ijkl\ldots} \left(B^{\mathrm{Sp},(\alpha\beta\ldots)}_{ijkl\ldots} - B^{\mathrm{FE},(\alpha\beta\ldots)}_{ijkl\ldots}\right)^2}}{\sqrt{\sum_{\alpha\beta\ldots,ijkl\ldots} (B^{\mathrm{FE},(\alpha\beta\ldots)}_{ijkl\ldots})^2}} \tag{42}$$

where $\boldsymbol{B}^{\mathrm{Sp}}$ is the quantity computed using the proposed spectral method and $\boldsymbol{B}^{\mathrm{FE}}$ is from the reference solution.

In all examples discussed below, the microstructures are taken to be made of face-centered cubic (FCC) polycrystals. The elastic properties are set to those for pure Aluminum: $C_{11} = 108.2$ GPa, $C_{12} = 61.3$ GPa, and $C_{44} = 28.5$ GPa. The phase property contrast comes from different crystal orientations of the phases within a polycrystal, unless otherwise stated.

4.1 2-grain and 10-grain microstructures

A 2-grain, layered polycrystal microstructure is considered first due to the simplicity of the geometry and, by extension, simplicity of the resulting response fields. The microstructure considered is shown in Fig. 1. The discretization consists of 125 voxels. The volume fractions of phases (1) and (2) are 60% and 40%, respectively. The orientations of the phases in terms of Bunge-Euler angles are given as (101.98, 145.03, 249.44) and (131.73, 86.26, 229.29) for phase one and two, respectively. The errors for the polarization and interaction tensors of the proposed method compared to the FEM solution are shown in Table 1. Homogenized moduli is given as

$$\overline{L}_{ijkl} = \frac{1}{|\Theta|} \int_{\Theta} A_{mnij}(\boldsymbol{y}) L_{mnab}(\boldsymbol{y}) A_{abkl}(\boldsymbol{y}) d\boldsymbol{y}. \tag{43}$$

The spectral method accurately computes the IFPs in this case, as evidenced by the small errors. Due to the simplified geometry, the polarization and interaction tensor fields are piecewise constant as observed in Fig 2.

A more complicated example with a 10-grain polycrystals is considered next to investigate the effect of mesh (i.e., voxel) size. Generated polycrystals are shown in Fig. 3. The microstructures are nearly identical, and discretized using 8,000, 15,625, and 125,000 voxels. The errors of the polarization and interaction tensors computed using the proposed spectral approach for all resolutions

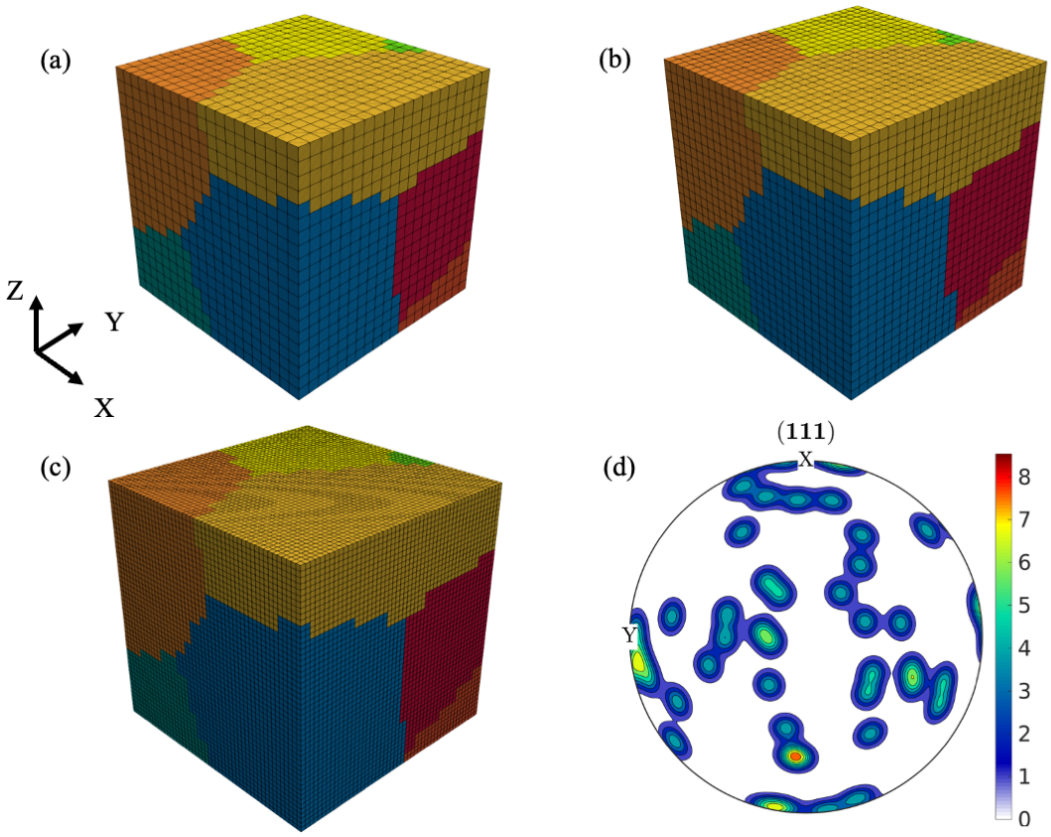

Figure 3: 10 grain polycrystal geometry with a) 8,000 voxels, b) 15,625 voxels, and c) 125,000 voxels, and d) pole figure showing grain orientations.

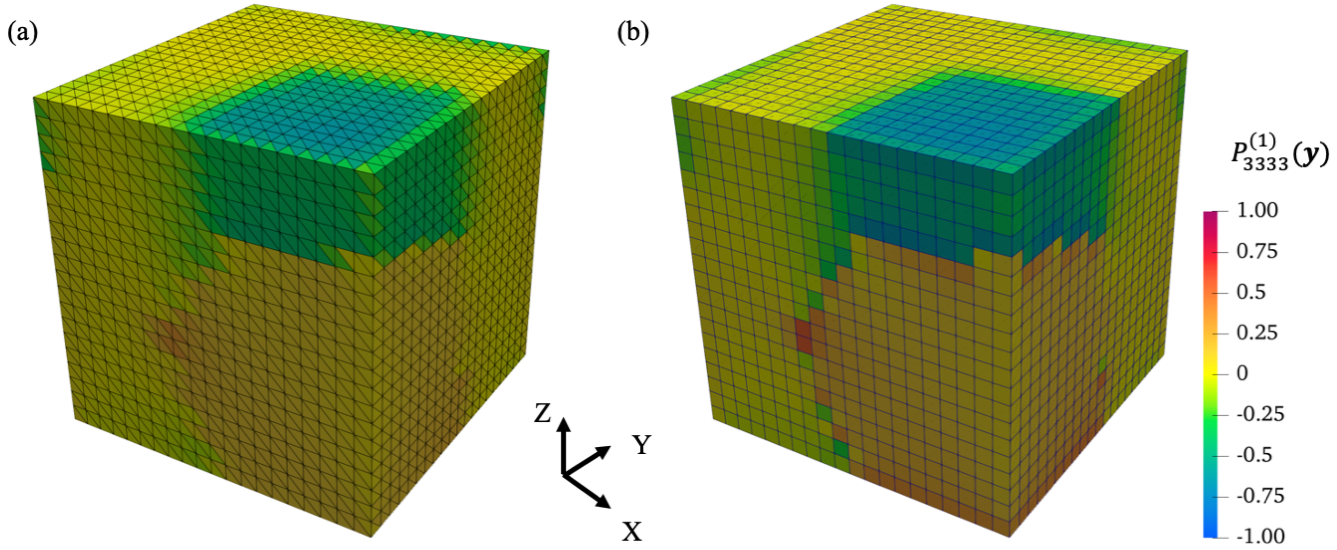

Figure 4: Interaction field $P^{(1)}_{3333}$ visualized over 10 grain polycrystal geometry with 8,000 voxels. Fields are computed using a) finite element and b) reduced order spectral methods.

are measured relative to the finest finite element solution (for 125,000 voxel problem) and are reported in Table 2.

The errors in the homogenized elastic stiffness tensor are negligible relative to the polarization and interaction tensors (approximately 0.01%). For all three quantities, the errors reduce with increased mesh refinement. When compared with the 2-grain microstructure, there is a marked increase in errors. The reason for the higher errors is the fact that localization and interaction tensor fields are no longer piecewise constant as shown in Fig. 4 and therefore reduced order approximation (piecewise constant approximation) does not recover exact fields. Still, the developed method captures essential features of the interaction field (compared to finite element solution) with some discrepancies in the grain boundary regions.

Although error measures give a sense of the accuracy of the method, a more consequential assessment could be made based on prediction of multiscale nonlinear responses using the ROM. To this end, the accuracy of the method is further assessed by comparing the ROM response using localization and interaction tensors computed from the spectral and the finite element methods.

We consider a cubic domain as the macroscopic structure. The domain is discretized using a single reduced-integration hexahedral element. The domain is subjected to six separate cases of monotonic loading as shown in the inset figures of Fig. 5. For each load case, 0.05 mm deformation is applied to the nodes shown in the Fig. 5a-f within a period of one second. The response of the 10-grain polycrystal is evaluated at the integration point at each increment of the nonlinear simulation. Viscoplastic flow rule and hardening rule as well as the viscoplastic properties for pure aluminum are used following Refs. [29, 58]. The resulting stress-strain response is shown in Fig. 5a-c for tensile tests and Fig. 5d-f for shear tests. The elastic-viscoplastic macroscopic response of the ROM using coefficient tensors from the spectral and the reference approaches are near identical for both tensile and shear tests. For completeness, microscale average Von Mises stress distribution ($\sigma^{(\beta)}$) for tensile loading in X direction is shown in Fig. 6. As observed from the figure, the errors in microscale stress distribution are minor suggesting that underlying reduced order approximation in the IFPs is not significantly affecting the performance of the reduced order model.

The computational efficiency of the proposed spectral method relative to the reference FEM for ROM construction was also studied. The computation time for the reference (t^{FE}) and the proposed (t^{Sp}) ROM construction stages are compared in Table 3 for the 10 grain polycrystal. For 125,000 voxels, the spectral code computes the coefficient tensors in approximately 23 seconds while the finite element code ran in approximately 5 hours, resulting in a speed-up of more than 800 fold. Majority of the finite element computation time is spent on constructing the stiffness matrix and computing the forcing vectors for each partition (i.e., right hand side in Eq. 40). Spectral code scales well with increasing grid size while increasing mesh size creates considerable decrease in efficiency of finite element code. For the discretization in the order of a half million voxels, the reference FE code is very expensive and the simulation did not complete within a reasonable period of time.

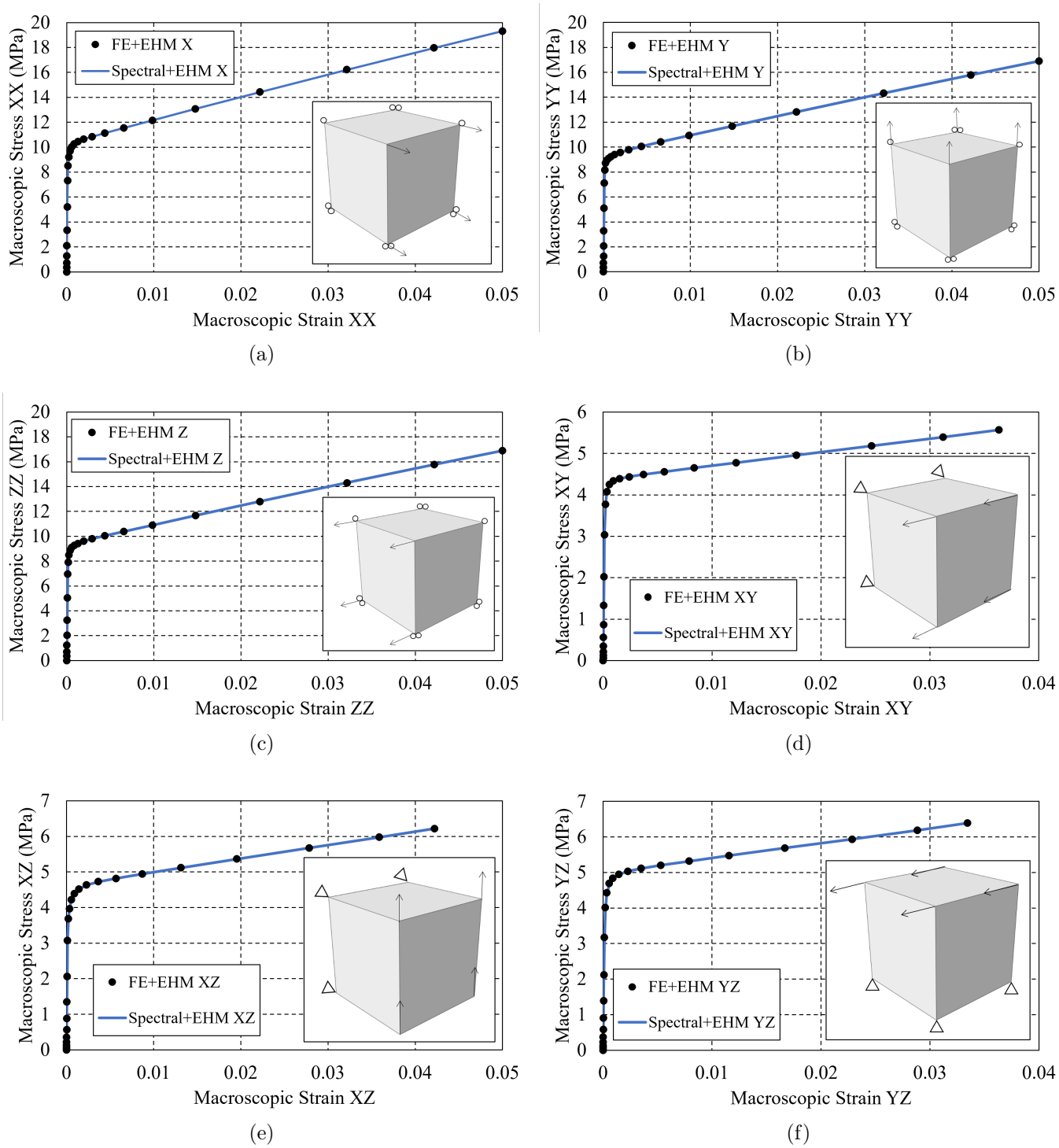

Figure 5: 10-grain polycrystal under monotonic a) tension in X, b) tension in Y, c) tension in Z, d) shear in XY, e) shear in XZ, and f) shear in YZ.

Voxel number	$e(\boldsymbol{G}^{(\beta)})$	$e(\boldsymbol{P}^{(\beta\alpha)})$	$e(\overline{\boldsymbol{L}})$
8,000	4.724 %	4.416 %	0.018 %
15,625	4.467 %	4.071 %	0.013 %
125,000	3.553 %	3.121 %	0.003 %

Table 2: 10-grain case: errors in localization and interaction tensors for the three grids considered.

Voxel number	t^{Sp}	t^{FE}	Speedup
8,000	9.23 s	130 s	14.08
15,625	10.25 s	383 s	37.36
125,000	23.18 s	18,727 s	808.03
512,000	95.86 s	-	-

Table 3: 10-grain case: total time spent on finite element and spectral simulations

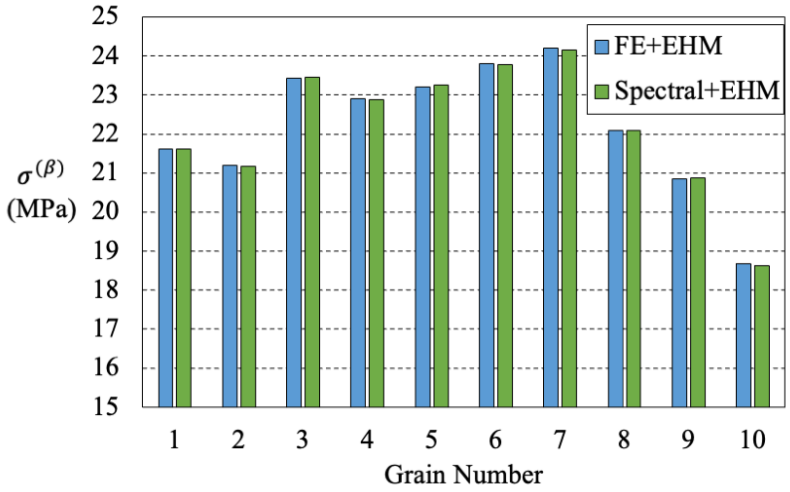

Figure 6: Comparison of microscale Von Mises stress ($\sigma^{(\beta)}$) distributions for 10-grain polycrystal under tensile loading in X direction at 5% strain.

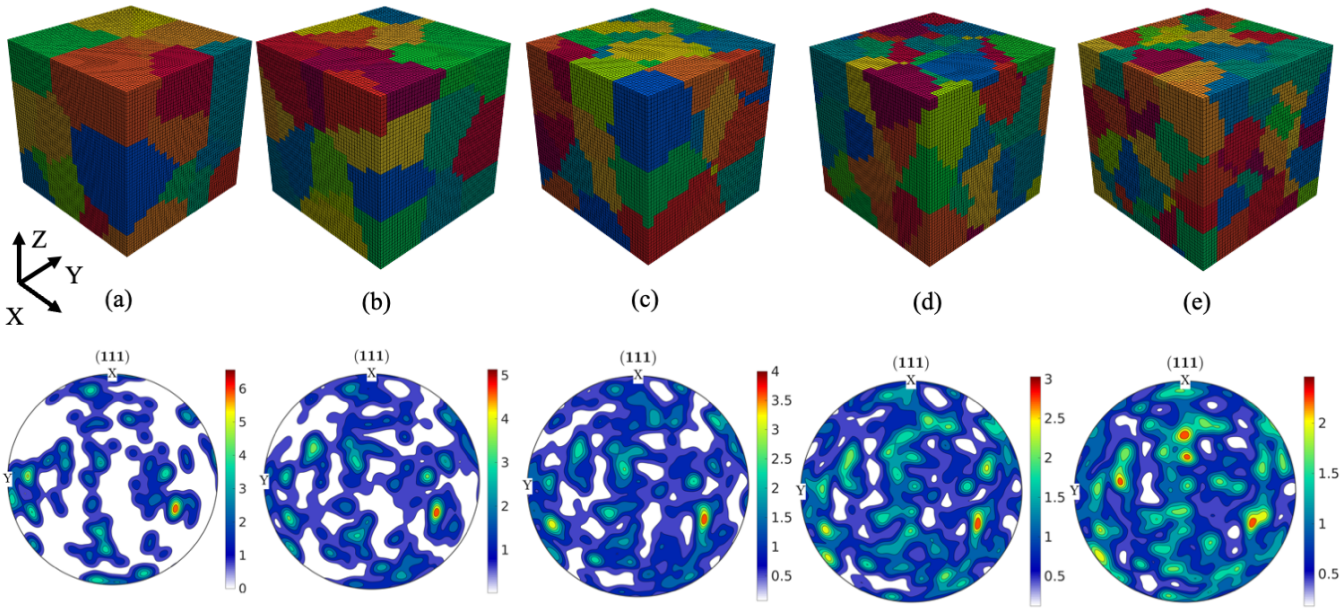

Figure 7: a) 25-grain polycrystal, b) 50-grain polycrystal, c) 75-grain polycrystal, d) 100-grain polycrystal, and e) 150-grain polycrystal.

4.2 Effect of microstructure size

The performance of spectral method is further assessed with increasing number of grains/ROM parts. Larger polycrystals with 25, 50, 75, 100, and 150 grains were generated as shown in Fig. 7. Total time consumed by the spectral method for constructing localization and interaction tensors is shown in Table 4. The number of voxels between the microstructures is kept approximately constant to the extent permitted by the microstructure generation software, Neper. For 100 grain polycrystal, it takes less than four minutes to construct the ROM, whereas in the reference simulation, memory limitation requires that computed solutions need to be transferred back-and-forth between the hard drive and the random access memory, drastically increasing the computation time. The accuracy of the method is similar to the case of 10-grain polycrystal. This result indicates that piecewise constant discretization is enough for constructing ROMs to sufficient accuracy for single-phase polycrystals. It is worth noting that for extreme number of phases or partitions in the microstructure, the efficiency of the spectral method should start to drop. This is due to the fact that resulting stiffness matrix (see Eq. 31 and Eq. 40) is dense. Therefore, for very large scale problems (e.g., >10,000 phases), it may be necessary to modify the proposed approach. For instance, enforcement of sparsity by neglecting certain interactions as proposed in Ref. [40] may provide efficiency enhancements. Matrix-free iterative methods, as described in Ref. [12, 3], offer an alternative approach in which convolutions are employed to perform matrix-vector products, thereby eliminating the requirement to store the stiffness matrix.

Grain number	t^{Sp}	t^{FE}	Voxel number	Speedup	$e(\boldsymbol{G}^{(\beta)})$	$e(\boldsymbol{P}^{(\beta\alpha)})$	$e(\overline{\boldsymbol{L}})$
25	26.0 s	33,256 s	157,464	612.3	3.885 %	3.540 %	0.002 %
50	86.5 s	18,574 s	117,649	254.9	3.191 %	3.510 %	0.001 %
75	120.0 s	19,268 s	117,649	160.6	4.458 %	4.530 %	0.004 %
100	210.7 s	208,533 s	157,464	989.8	4.381 %	4.497 %	0.003 %
150	339.0 s	-	117,649	-	-	-	-

Table 4: Scaling of the spectral method with increasing number of grains.

r	$e(\boldsymbol{G}^{(\beta)})$	$e(\boldsymbol{P}^{(\beta\alpha)})$	$e(\overline{\boldsymbol{L}})$
1	4.467 %	4.071 %	0.013 %
2	6.254 %	5.167 %	0.095 %
5	8.699 %	7.210 %	0.235 %
10	16.345 %	13.657 %	1.541 %

Table 5: Errors of polarization and interaction tensors with changing value of contrast ratio, r.

4.3 Effect of phase contrast

Heterogeneity in the polycrystalline materials is induced by the differences in the elastic modulus along different crystal orientations. For most materials, the property contrast between neighboring crystals is relatively low. Higher property contrasts can develop due to the presence of additional hard/soft phases in the microstructure. For example, α and β phases in titanium alloys have phase contrast of approximately two in crystal coordinate system [41, 59]. Phase contrast can reach 40-50 for other cases such as polymer composite materials reinforced with carbon fibers [60, 61].

In this section, we study the effect of phase property contrast on the accuracy of the spectral method. To construct such an example, the 10-grain polycrystal discretized using 15,625 voxels is used. High property contrast is introduced into the microstructure by rescaling the elastic constants of a grain near the center of the microstructure volume shown in Fig 8. Specifically, we increase the cubic elastic constants using following formulas $\hat{C}_{11} = rC_{11}$, $\hat{C}_{12} = rC_{12}$, and $\hat{C}_{44} = rC_{44}$ where r is the contrast ratio. The errors in polarization and interaction tensors are shown in Table 5. Errors for homogenized moduli appear to be relatively small for all phase contrasts considered. However, accuracy of polarization and interaction tensors decreases with increasing value of r indicating effect of higher phase contrast on the accuracy of the spectral method. We also report the response of the ROM for the phase contrast of $r = 10$ under tensile loading as shown in Fig. 9. Although macroscale response of the ROM and microscale average Von Mises stresses are indistinguishable,

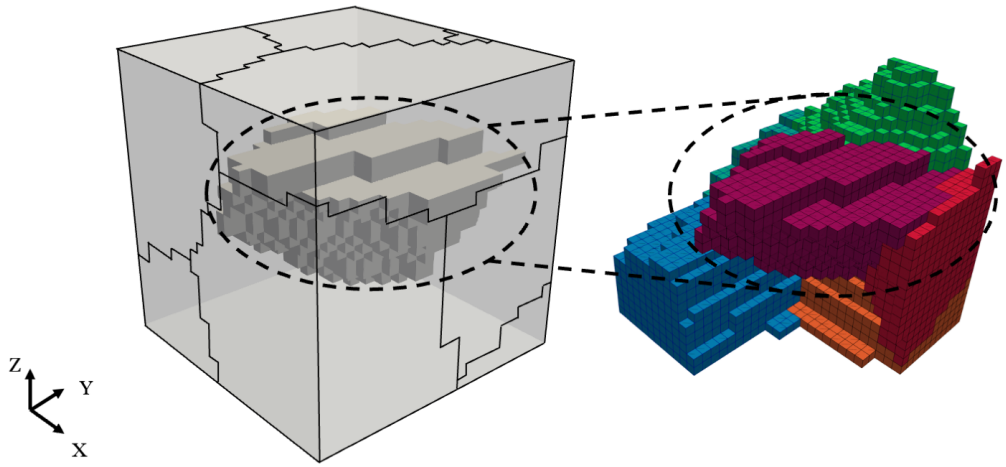

Figure 8: 10-grain polycrystal (transparent) with high-contrast grain in the center.

there are higher errors observed in individual microscale average stress component $\sigma_{11}^{(\beta)}$. The highest error of about 4.8% occurs in microscale stresses of grain 10 which is the grain with elevated elastic constants. There are two levels of discretizations that are used in the reduced order spectral method: a regular voxel grid for FFT algorithms and piecewise uniform partitioning for incompatible strain fields. Majority of the discrepancy observed for increasing phase contrast is coming from coarse discretization of the incompatible strain fields (Eq. 25) and can be controlled in a similar way to finite element discretizations. For instance, using more partitions around regions with high phase contrast (similar to h-refinement) or using higher order basis functions to represent the variation of the strain fields with the partitions (similar to p-refinement) could mitigate the errors associated with high property contrasts. High phase contrast could also amplify the Gibbs phenomenon necessitating introduction of modified projection operators as discussed in Ref. [8].

5 Conclusion

A reduced order spectral method for computation of localization and interaction tensors for reduced order computational homogenization was developed. The proposed method does not make any assumption regarding the geometry of the phases, phase-to-phase interactions, or the introduction of a reference stiffness parameter. The accuracy of macro and micro-scale quantities of the proposed method has been demonstrated for singe-phase polycrystals indicating sufficiency of the reduced order approximation. Proposed method achieves a speedup of higher than an order of magnitude over finite element method.

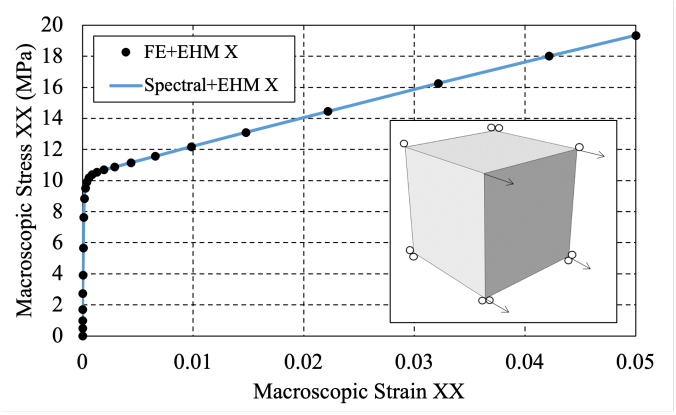

(a)

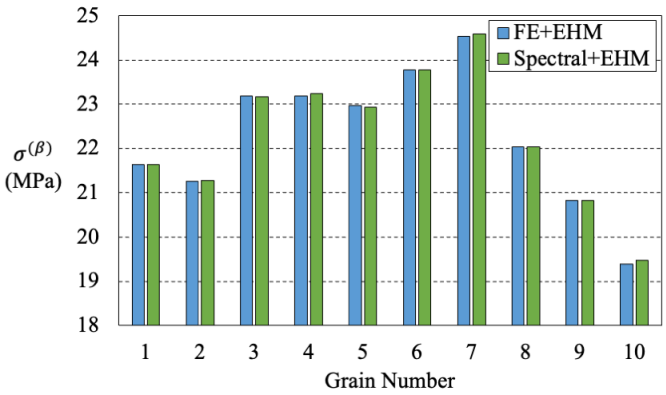

(b)

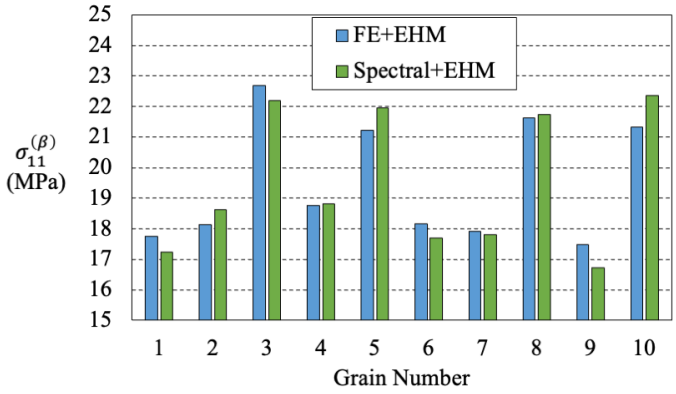

(c)

Figure 9: Comparison of a) macroscale stress-strain response of a 10 grain polycrystal (with contrast of $r = 10$) under tensile loading in X direction for ROM constructed using FE and spectral methods, b) corresponding microscale grain-wise average Von Mises stresses ($\sigma^{(\beta)}$) at 5% strain and c) corresponding microscale grain-wise average normal stresses ($\sigma_{11}^{(\beta)}$) at 5% strain.

On the other hand, accuracy of the method decreases with increasing phase contrast. This issue can be addressed by adding additional degrees of freedom with the advantage of using non-uniform basis functions without restriction to elementary (finite-element type) geometries [18, 22, 19]. Further, the scalability of the method degrades with increasing number of partitions due to storage and lack of efficient algorithms for dense linear systems. However, iterative methods in conjunction with FFT algorithms for convolutions could be used to improve efficiency of the method [12].

6 Acknowledgements

The authors gratefully acknowledge the financial support from National Aeronautics and Space Administration (NASA), Space Technology Early State Innovation (ESI) Grant (No.:80NSS C20K0294).

Appendix A Derivation of the compatibility operator

The resulting expression for the compatibility operator is stated by Milton and Kohn [14]. For completeness, we provide one way to arrive at the resulting expression. Consider Helmholtz decomposition for a generalized polarization strain tensor given as

$$G^{\star}_{ijmn}(\boldsymbol{y}) = G_{ijmn}(\boldsymbol{y}) + G^{divfree}_{ijmn}(\boldsymbol{y}) + \overline{G}_{ijmn} \tag{44}$$

where first term is curl-free (compatible) zero-mean field, second term is divergence-free (incompatible) zero-mean field, and third term is a constant field representing the average. The operator $\boldsymbol{\Gamma}$ needs to be constructed such that a generalized polarization strain tensor, $\boldsymbol{G}^{\star}$, is mapped into its compatible zero-mean part, $\boldsymbol{G}$. Note that divergence of both sides is given by $\nabla \cdot \boldsymbol{G}^{\star} = \nabla \cdot \boldsymbol{G}$. On the other hand, by definition of $\boldsymbol{G}$ we have $\nabla \times \boldsymbol{G} = 0$. One can use these two properties to establish a relationship between the whole tensor, $\boldsymbol{G}^{\star}$, and the curl-free zero-mean part, $\boldsymbol{G}$. The classical compatibility relationship can be written as follows

$$G_{ab,cd} - G_{cb,ad} - G_{ad,cb} + G_{cd,ab} = 0. \tag{45}$$

Note that indices m and n have been dropped for the sake of compactness. The divergence with respect to a and b indices is given by

$$G_{ab,cdab} - G_{cb,adab} - G_{ad,cbab} + G_{cd,abab} = 0. \tag{46}$$

The expression above can be transformed to frequency space such that

$$\hat{G}_{ab}\xi_c\xi_d\xi_a\xi_b - \hat{G}_{cb}\xi_b\xi_d||\xi||^2 - \hat{G}_{ad}\xi_c\xi_a||\xi||^2 + \hat{G}_{cd}||\xi||^4 = 0. \tag{47}$$

Note that the $\boldsymbol{G}$ tensor in the first three terms can be replaced with $\boldsymbol{G}^{\star}$ due to divergence relationship given earlier such that

$$\hat{G}^{\star}_{ab}\xi_c\xi_d\xi_a\xi_b - \hat{G}^{\star}_{cb}\xi_b\xi_d||\xi||^2 - \hat{G}^{\star}_{ad}\xi_c\xi_a||\xi||^2 + \hat{G}_{cd}||\xi||^4 = 0. \tag{48}$$

We can then isolate the curl-free part and express it in terms of $\boldsymbol{G}^{\star}$ as

$$\hat{G}_{cd} = \frac{1}{||\xi||^2}(\hat{G}^{\star}_{cb}\xi_b\xi_d + \hat{G}^{\star}_{ad}\xi_c\xi_a) - \frac{1}{||\xi||^4}\hat{G}^{\star}_{ab}\xi_c\xi_d\xi_a\xi_b. \tag{49}$$

Considering symmetry of $\hat{\boldsymbol{G}}^{\star}$ one can rewrite the following relationship as

$$\hat{G}_{cd} = \left[\frac{1}{2||\xi||^2}(\delta_{ca}\xi_b\xi_d + \delta_{cb}\xi_a\xi_d + \delta_{bd}\xi_c\xi_a + \delta_{ad}\xi_c\xi_b) - \frac{1}{||\xi||^4}\xi_c\xi_d\xi_a\xi_b\right]\hat{G}^{\star}_{ab} \tag{50}$$

$$\hat{G}_{cd} = \hat{\Gamma}_{cdab}\hat{G}^{\star}_{ab} \tag{51}$$

where the operator $\boldsymbol{\Gamma}$ acts as a map into zero-mean compatible space of strains. Using the convolution theorem, we can rewrite the result in real space as

$$G_{cd} = \Gamma_{cdab} * G^{\star}_{ab}. \tag{52}$$

References

[1] F. Feyel and J.L. Chaboche. "FE2 multiscale approach for modelling the elastoviscoplastic behaviour of long fibre SiC/Ti composite materials". In: *Computer Methods in Applied Mechanics and Engineering* 183 (2000), pp. 309–330.

[2] M. Marino, B. Hudobivnik, and P. Wriggers. "Computational homogenization of polycrystalline materials with the Virtual Element Method". In: *Computer Methods in Applied Mechanics and Engineering* 355 (2019), pp. 349–372. ISSN: 0045-7825. DOI: https://doi.org/10.1016/j.cma.2019.06.004. URL: https://www.sciencedirect.com/science/article/pii/S0045782519303445.

[3] H. Moulinec and P. Suquet. "A numerical method for computing the overall response of nonlinear composites with complex microstructure". In: *Computer Methods in Applied Mechanics and Engineering* 157.1 (1998), pp. 69–94. ISSN: 0045-7825. DOI: https://doi.org/10.1016/S0045-7825(97)00218-1. URL: https://www.sciencedirect.com/science/article/pii/S0045782597002181.

[4] S. Lucarini and J. Segurado. "DBFFT: A displacement based FFT approach for non-linear homogenization of the mechanical behavior". In: *International Journal of Engineering Science* 144 (2019), p. 103131. ISSN: 0020-7225. DOI: https://doi.org/10.1016/j.ijengsci.2019.103131.

[5] J.C. Michel, H. Moulinec, and P. Suquet. "Effective properties of composite materials with periodic microstructure: a computational approach". In: *Computer Methods in Applied Mechanics and Engineering* 172.1 (1999), pp. 109–143. ISSN: 0045-7825. DOI: https://doi.org/10.1016/S0045-7825(98)00227-8. URL: https://www.sciencedirect.com/science/article/pii/S0045782598002278.

[6] F. S. Göküzüm, L. T. K. Nguyen, and M. Keip. "A multiscale FE-FFT framework for electroactive materials at finite strains". In: *Computational mechanics* 64 (2019), pp. 63–84.

[7] J. Michel, H. Moulinec, and P. Suquet. "A computational scheme for linear and non-linear composites with arbitrary phase contrast". In: *International Journal for Numerical Methods in Engineering* 52 (Sept. 2001), pp. 139–160. DOI: 10.1002/nme.275.

[8] F. Willot. "Fourier-based schemes for computing the mechanical response of composites with accurate local fields". In: *Comptes Rendus Mécanique* 343.3 (2015), pp. 232–245. ISSN: 1631-0721. DOI: https://doi.org/10.1016/j.crme.2014.12.005. URL: https://www.sciencedirect.com/science/article/pii/S1631072114002149.

[9] S. Lucarini, M. V. Upadhyay, and J. Segurado. "FFT based approaches in micromechanics: fundamentals, methods and applications". In: *Modelling and Simulation in Materials Science and Engineering* 30.2 (2021), p. 023002. DOI: 10.1088/1361-651X/ac34e1. URL: https://dx.doi.org/10.1088/1361-651X/ac34e1.

[10] R. A. Lebensohn and A.D. Rollett. "Spectral methods for full-field micromechanical modelling of polycrystalline materials". In: *Computational Materials Science* 173 (2020), p. 109336. ISSN: 0927-0256. DOI: https://doi.org/10.1016/j.commatsci.2019.109336. URL: https://www.sciencedirect.com/science/article/pii/S0927025619306354.

[11] M. Schneider. "A review of nonlinear FFT-based computational homogenization methods". In: *Acta Mechanica* 232.6 (2021), pp. 2051–2100.

[12] J. Zeman et al. "A finite element perspective on nonlinear FFT-based micromechanical simulations". In: *International Journal for Numerical Methods in Engineering* 111.10 (2017), pp. 903–926. DOI: https://doi.org/10.1002/nme.5481. eprint: https://onlinelibrary.wiley.com/doi/pdf/10.1002/nme.5481. URL: https://onlinelibrary.wiley.com/doi/abs/10.1002/nme.5481.

[13] T.W.J. de Geus et al. "Finite strain FFT-based non-linear solvers made simple". In: *arXiv preprint arXiv:1603.08893* (2016).

[14] G. W. Milton and R. V. Kohn. "Variational bounds on the effective moduli of anisotropic composites". In: *Journal of the Mechanics and Physics of Solids* 36.6 (1988), pp. 597–629. ISSN: 0022-5096. DOI: https://doi.org/10.1016/0022-5096(88)90001-4. URL: https://www.sciencedirect.com/science/article/pii/0022509688900014.

[15] G. J. Dvorak and Y. Benveniste. "On Transformation Strains and Uniform Fields in Multiphase Elastic Media". In: *Proceedings: Mathematical and Physical Sciences* 437.1900 (1992), pp. 291–310. ISSN: 09628444. URL: http://www.jstor.org/stable/52199 (visited on 08/22/2022).

[16] G. J. Dvorak. "Transformation field analysis of inelastic composite materials". In: *Proceedings of the Royal Society of London. Series A: Mathematical and Physical Sciences* 437.1900 (1992), pp. 311–327. DOI: 10.1098/rspa.1992.0063. eprint: https://royalsocietypublishing.org/doi/pdf/10.1098/rspa.1992.0063. URL: https://royalsocietypublishing.org/doi/abs/10.1098/rspa.1992.0063.

[17] J.C. Michel and P. Suquet. "Computational analysis of nonlinear composite structures using the nonuniform transformation field analysis". In: *Computer Methods in Applied Mechanics and Engineering* 193.48 (2004). Advances in Computational Plasticity, pp. 5477–5502. ISSN: 0045-7825. DOI: https://doi.org/10.1016/j.cma.2003.12.071. URL: https://www.sciencedirect.com/science/article/pii/S004578250400283X.

[18] J.C. Michel and P. Suquet. "Nonuniform transformation field analysis". In: *International Journal of Solids and Structures* 40.25 (2003). Special issue in Honor of George J. Dvorak, pp. 6937–6955. ISSN: 0020-7683. DOI: https://doi.org/10.1016/S0020-7683(03)00346-9. URL: https://www.sciencedirect.com/science/article/pii/S0020768303003469.

[19] F. Covezzi et al. "Comparison of reduced order homogenization techniques: pRBMOR, NUTFA and MxTFA". In: *Meccanica* 53 (2018), pp. 1291–1312.

[20] F. Fritzen, S. Marfia, and V. Sepe. "Reduced order modeling in nonlinear homogenization: A comparative study". In: *Computers & Structures* 157 (2015), pp. 114–131. ISSN: 0045-7949. DOI: https://doi.org/10.1016/j.compstruc.2015.05.012. URL: https://www.sciencedirect.com/science/article/pii/S0045794915001492.

[21] F. Fritzen and M. Leuschner. "Reduced basis hybrid computational homogenization based on a mixed incremental formulation". In: *Computer Methods in Applied Mechanics and Engineering* 260 (2013), pp. 143–154. ISSN: 0045-7825. DOI: https://doi.org/10.1016/j.cma.2013.03.007. URL: https://www.sciencedirect.com/science/article/pii/S0045782513000583.

[22] V. Sepe, S. Marfia, and E. Sacco. "A nonuniform TFA homogenization technique based on piecewise interpolation functions of the inelastic field". In: *International Journal of Solids and Structures* 50.5 (2013), pp. 725–742. ISSN: 0020-7683. DOI: https://doi.org/10.1016/j.ijsolstr.2012.11.005. URL: https://www.sciencedirect.com/science/article/pii/S0020768312004684.

[23] F. Covezzi et al. "Homogenization of elastic–viscoplastic composites by the Mixed TFA". In: *Computer Methods in Applied Mechanics and Engineering* 318 (2017), pp. 701–723. ISSN: 0045-7825. DOI: https://doi.org/10.1016/j.cma.2017.02.009. URL: https://www.sciencedirect.com/science/article/pii/S0045782516308635.

[24] J. Yvonnet, D. Gonzalez, and Q.-C. He. "Numerically explicit potentials for the homogenization of nonlinear elastic heterogeneous materials". In: *Computer Methods in Applied Mechanics and Engineering* 198.33 (2009), pp. 2723–2737. ISSN: 0045-7825. DOI: https://doi.org/10.1016/j.cma.2009.03.017. URL: https://www.sciencedirect.com/science/article/pii/S0045782509001492.

[25] Z. Liu, M.A. Bessa, and W. K. Liu. "Self-consistent clustering analysis: An efficient multi-scale scheme for inelastic heterogeneous materials". In: *Computer Methods in Applied Mechanics and Engineering* 306 (2016), pp. 319–341. ISSN: 0045-7825. DOI: https://doi.org/10.1016/j.cma.2016.04.004. URL: https://www.sciencedirect.com/science/article/pii/S0045782516301499.

[26] C. Oskay and J. Fish. "Eigendeformation-based reduced order homogenization for failure analysis of heterogeneous materials". In: *Computer Methods in Applied Mechanics and Engineering* 196.7 (2007), pp. 1216–1243. ISSN: 0045-7825. DOI: https://doi.org/10.1016/j.cma.2006.08.015. URL: https://www.sciencedirect.com/science/article/pii/S0045782506002933.

[27] Z. Yuan and J. Fish. "Multiple scale eigendeformation-based reduced order homogenization". In: *Computer Methods in Applied Mechanics and Engineering* 198.21 (2009). Advances in Simulation-Based Engineering Sciences – Honoring J. Tinsley Oden, pp. 2016–2038. ISSN: 0045-7825. DOI: https://doi.org/10.1016/j.cma.2008.12.038. URL: https://www.sciencedirect.com/science/article/pii/S0045782509000243.

[28] R. D. Crouch and C. Oskay. "Symmetric meso-mechanical model for failure analysis of heterogeneous materials". In: *Int. J. Mult. Comp. Eng.* 8 (2010), pp. 447–461.

[29] X. Zhang and C. Oskay. "Eigenstrain based reduced order homogenization for polycrystalline materials". In: *Computer Methods in Applied Mechanics and Engineering* 297 (2015), pp. 408–436. ISSN: 0045-7825. DOI: https://doi.org/10.1016/j.cma.2015.09.006. URL: https://www.sciencedirect.com/science/article/pii/S004578251500300X.

[30] D. Xia, X. Zhang, and C. Oskay. "Large-deformation reduced order homogenization of polycrystalline materials". In: *Computer Methods in Applied Mechanics and Engineering* 387 (2021), p. 114119. ISSN: 0045-7825. DOI: https://doi.org/10.1016/j.cma.2021.114119. URL: https://www.sciencedirect.com/science/article/pii/S0045782521004503.

[31] D. Xia and C. Oskay. "Reduced order mathematical homogenization method for polycrystalline microstructure with microstructurally small cracks". In: *International Journal for Numerical Methods in Engineering* 124.14 (2023), pp. 3166–3190. DOI: https://doi.org/10.1002/nme.7243. eprint: https://onlinelibrary.wiley.com/doi/pdf/10.1002/nme.7243. URL: https://onlinelibrary.wiley.com/doi/abs/10.1002/nme.7243.

[32] J. Fish et al. "Computational plasticity for composite structures based on mathematical homogenization: Theory and practice". In: *Computer Methods in Applied Mechanics and Engineering* 148.1 (1997), pp. 53–73. ISSN: 0045-7825.

[33] V. Minh Nguyen-Thanh et al. "A surrogate model for computational homogenization of elastostatics at finite strain using high-dimensional model representation-based neural network". In: *International Journal for Numerical Methods in Engineering* 121.21 (2020), pp. 4811–4842. DOI: https://doi.org/10.1002/nme.6493. eprint: https://onlinelibrary.wiley.com/doi/pdf/10.1002/nme.6493. URL: https://onlinelibrary.wiley.com/doi/abs/10.1002/nme.6493.

[34] R. Hatano et al. "FE^{2r} method with surrogate localization model for hyperelastic composite materials". In: *Advanced Modeling and Simulation in Engineering Sciences* 7.1 (2020), p. 39. ISSN: 2213-7467. DOI: 10.1186/s40323-020-00175-0. URL: https://doi.org/10.1186/s40323-020-00175-0.

[35] J. N. Fuhg, M. Marino, and N. Bouklas. "Local approximate Gaussian process regression for data-driven constitutive models: development and comparison with neural networks". In: *Computer Methods in Applied Mechanics and Engineering* 388 (2022), p. 114217. ISSN: 0045-7825. DOI: https://doi.org/10.1016/j.cma.2021.114217. URL: https://www.sciencedirect.com/science/article/pii/S004578252100548X.

[36] P. Krysl, S. Lall, and J. E. Marsden. "Dimensional model reduction in non-linear finite element dynamics of solids and structures". In: *International Journal for Numerical Methods in Engineering* 51.4 (2001), pp. 479–504. DOI: https://doi.org/10.1002/nme.167. eprint: https://onlinelibrary.wiley.com/doi/pdf/10.1002/nme.167. URL: https://onlinelibrary.wiley.com/doi/abs/10.1002/nme.167.

[37] J. Yvonnet and Q.-C. He. "The reduced model multiscale method (R3M) for the non-linear homogenization of hyperelastic media at finite strains". In: *Journal of Computational Physics* 223.1 (2007), pp. 341–368. ISSN: 0021-9991. DOI: https://doi.org/10.1016/j.jcp.2006.09.019. URL: https://www.sciencedirect.com/science/article/pii/S0021999106004402.

[38] D. Xia and C. Oskay. "Proper orthogonal decomposition assisted eigendeformation-based mathematical homogenization method for modeling cracks in 3D polycrystalline microstructures". In: *Comput. Meth. Appl. Mech. Engrg.* 418 (2024), p. 116508.

[39] M. Ohlberger and S. Rave. "Reduced Basis Methods: Success, Limitations and Future Challenges". In: *arXiv: Numerical Analysis* (2015). URL: https://api.semanticscholar.org/CorpusID:62791143.

[40] X. Zhang and C. Oskay. "Sparse and scalable eigenstrain-based reduced order homogenization models for polycrystal plasticity". In: *Computer Methods in Applied Mechanics and Engineering* 326 (2017), pp. 241–269. ISSN: 0045-7825. DOI: https://doi.org/10.1016/j.cma.2017.07.027. URL: https://www.sciencedirect.com/science/article/pii/S004578251730347X.

[41] X. Zhang, Y. Liu, and C. Oskay. "Uncertainty Quantification for Microstructure-Sensitive Fatigue Nucleation and Application to Titanium Alloy, Ti6242". In: *Frontiers in Materials* 9, 897998 (May 2022), p. 897998. DOI: 10.3389/fmats.2022.897998.

[42] D. R. Brandyberry, X. Zhang, and P. H. Geubelle. "A GFEM-based reduced-order homogenization model for heterogeneous materials under volumetric and interfacial damage". In: *Computer Methods in Applied Mechanics and Engineering* 377 (2021), p. 113690. ISSN: 0045-7825. DOI:

https://doi.org/10.1016/j.cma.2021.113690. URL: https://www.sciencedirect.com/science/article/pii/S0045782521000268.

[43] A. Nasirov et al. "Achieving high efficiency in reduced order modeling for large scale polycrystal plasticity simulations". In: *Finite Elements in Analysis and Design* 228 (2024), p. 104053. ISSN: 0168-874X. DOI: https://doi.org/10.1016/j.finel.2023.104053. URL: https://www.sciencedirect.com/science/article/pii/S0168874X23001464.

[44] V. A. Buryachenko. "Transformation field analysis as a background of clustering discretization methods in micromechanics of composites". In: *Mathematics and Mechanics of Solids* 0.0 (0), p. 10812865231174219. DOI: 10.1177/10812865231174219. eprint: https://doi.org/10.1177/10812865231174219. URL: https://doi.org/10.1177/10812865231174219.

[45] T. Mori and K. Tanaka. "Average stress in matrix and average elastic energy of materials with misfitting inclusions". In: *Acta Metallurgica* 21.5 (1973), pp. 571–574. ISSN: 0001-6160. DOI: https://doi.org/10.1016/0001-6160(73)90064-3. URL: https://www.sciencedirect.com/science/article/pii/0001616073900643.

[46] Y. Benveniste. "A new approach to the application of Mori-Tanaka's theory in composite materials". In: *Mechanics of Materials* 6.2 (1987), pp. 147–157. ISSN: 0167-6636. DOI: https://doi.org/10.1016/0167-6636(87)90005-6.

[47] X. Zhang, Y. Liu, and C. Oskay. "Multiscale reduced-order modeling of a titanium skin panel subjected to thermomechanical loading". In: *AIAA Journal* 60.1 (2022), pp. 302–315.

[48] X. Zhang, Y. Liu, and C. Oskay. "Uncertainty quantification for microstructure-sensitive fatigue nucleation and application to titanium alloy, Ti6242". In: *Frontiers in Materials* 9 (2022), p. 897998.

[49] X. Zhang and C. Oskay. "Polycrystal plasticity modeling of nickel-based superalloy IN 617 subjected to cyclic loading at high temperature". In: *Modelling Simul. Mater. Sci. Eng.* 24.055009 (2016).

[50] V. -T. Phan et al. "Microscale modeling of creep deformation and rupture in Nickel-based superalloy IN 617 at high temperature". In: *Mech. Mater.* 114 (2017), pp. 215–227.

[51] X. Zhang and C. Oskay. "Plastic dissipation sensitivity to mechanical properties in polycrystalline β-HMX subjected to impact loading". In: *Mech. Mater.* 138 (2019), p. 103079.

[52] X. Zhang and C. Oskay. "Modeling and numerical investigation of mechanical twinning in β-HMX crystals subjected to shock loading". In: *Modelling Simul. Mater. Sci. Eng.* 29 (2021), p. 075009.

[53] Y. C. Fung and P. Tong. *Classical and computational solid mechanics*. eng. Advanced series in engineering science ; v. 1. Singapore ; River Edge, NJ: World Scientific, 2001. ISBN: 9810241240.

[54] R. Quey and M. Kasemer. "The Neper/FEPX Project: Free / Open-source Polycrystal Generation, Deformation Simulation, and Post-processing". In: *IOP Conference Series: Materials Science and Engineering* 1249.1 (2022), p. 012021. DOI: 10.1088/1757-899X/1249/1/012021. URL: https://dx.doi.org/10.1088/1757-899X/1249/1/012021.

[55] C. R. Harris et al. "Array programming with NumPy". In: *Nature* 585.7825 (Sept. 2020), pp. 357–362. DOI: 10.1038/s41586-020-2649-2. URL: https://doi.org/10.1038/s41586-020-2649-2.

[56] P. Virtanen et al. "SciPy 1.0: Fundamental Algorithms for Scientific Computing in Python". In: *Nature Methods* 17 (2020), pp. 261–272. DOI: 10.1038/s41592-019-0686-2.

[57] S. K. Lam, A. Pitrou, and S. Seibert. "Numba: A llvm-based python jit compiler". In: *Proceedings of the Second Workshop on the LLVM Compiler Infrastructure in HPC*. 2015, pp. 1–6.

[58] E. B. Marin. "On the formulation of a crystal plasticity model." In: (Aug. 2006). DOI: 10.2172/890604. URL: https://www.osti.gov/biblio/890604.

[59] Y. He et al. "Fabrication, Structure, and Mechanical and Ultrasonic Properties of Medical Ti6Al4V Alloys Part II: Relationship between Microstructure and Mechanical Properties and Ultrasonic Properties of Ultrasonic Scalpel". In: *Materials* 13 (Jan. 2020), p. 284. DOI: 10.3390/ma13020284.

[60] Z. Su and C. Oskay. "Mesh size objective fatigue damage propagation in laminated composites using the multiscale discrete damage theory". In: *Computational Mechanics* 67 (2021), pp. 969–987.

[61] Z. Su and C. Oskay. "Modeling arbitrarily oriented and reorienting multiscale cracks in composite materials with adaptive multiscale discrete damage theory". In: *Computational Mechanics* 70.5 (2022), pp. 1041–1058.